



LDA measurements in a one-sided ribbed square channel at Reynolds numbers of 50,000 and 100,000

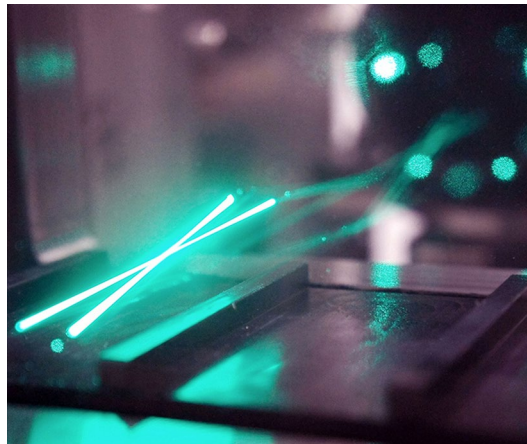
Sebastian Ruck¹ · Frederik Arbeiter¹

Received: 29 June 2021 / Revised: 19 August 2021 / Accepted: 13 September 2021 / Published online: 20 October 2021
© The Author(s) 2021

Abstract

Laser Doppler anemometry (LDA) measurements in the fully developed turbulent flow through a one-sided rib-roughened square channel with a rib-height-to-channel-height ratio of $k/H = 0.0667$ and a rib-pitch-to-rib-height ratio of $p/k = 9$ were carried out at Reynolds numbers (based on the channel height H and the mean bulk velocity u_B) of $Re_H = 5.0 \cdot 10^4$ and $1.0 \cdot 10^5$. Mean velocities, Reynolds normal, and shear stresses were determined. The first- and second-order statistical moments of the velocity differed slightly between both Reynolds numbers when normalized by the bulk velocity and the channel height. Deviations were attributed to a minor elongation increase in the large recirculation region behind the rib with increasing Reynolds numbers. The crucial role of turbulent diffusion was reflected in the non-coincidence of the maximum primary mean shear and the Reynolds normal stress as well as outward drifts of the Reynolds stress peaks along the rib crest. Turbulent diffusion contributed significantly to the turbulence kinetic energy (*TKE*) budget near the rib crest and within the separated shear layer, while mean convection made a remarkable contribution only at the rib leading edge. The detailed first- and second-order moments provide a basis for the validation of computational methods and turbulence models.

Graphic abstract



1 Introduction

Attached ribs are an appropriate surface structure for increasing the heat transfer in the cooling ducts of gas turbine blades (Han 2004), solar receivers (Hans et al. 2009), or thermally highly loaded reactor components (Ruck et al. 2019). Fundamental research about turbulent flows over walls roughened by transverse ribs of the height k has been

✉ Sebastian Ruck
sebastian.ruck@kit.edu

¹ Institute of Neutron Physics and Reactor Technology, Karlsruhe Institute of Technology, Hermann-von-Helmholtz-Platz 1, 76344 Eggenstein-Leopoldshafen, Germany

carried out for decades. Different rib-pitch-to-rib-height ratios p/k produce different flow patterns, and the flow field around the ribs can be divided into an inner roughness layer where the flow is affected by length scales associated with the roughness and into an undisturbed outer region (e.g., Raupach et al. 1991). The flow field of the k -type roughness (Perry et al. 1969) provides an effective fluid mixing and is of high importance to thermally highly loaded heat exchanger components. Therefore, rib configurations reproducing flow characteristics of the k -type roughness are often applied to rectangular or square cooling channels (Liou et al. 1992; Rau et al. 1998; Casarsa and Arts 2005; Labbé 2013). In the following section, some literature about turbulent flow in ribbed rectangular or square channels relevant to the present study is reviewed briefly.

Hirota et al. (1992) systematically carried out hotwire anemometry measurements in one- and two-sided rib-roughened square channels ($p/k = 10$, $k/H = 0.02$) at a Reynolds number of $Re_H = 6.5 \cdot 10^4$. Their results showed that the core flow region was dominated by a secondary flow structure of two large counter-rotating vortices in the spanwise-wall-normal plane which transported fluid downwards at the channel center and upwards near the adjacent smooth side walls. Liou et al. (1993) analysed the structure of the turbulent flow field in a two-sided, opposite rib-roughened rectangular channel with a width W and height H [$p/k = 10$, $k/D_h = 0.133$ and $H/W = 0.5$ with the hydraulic diameter $D_h = 4 \cdot H \cdot W / (2 \cdot (H + W))$] at a Reynolds number (based on D_h and u_B) of $Re_{D_h} = 3.3 \cdot 10^4$. They found that the secondary flow was triggered by the anisotropy of the flow field which was indicated by strongly direction-dependent velocity fluctuations, and thus, the secondary flow was classified as the Prandtl's secondary flow of the second kind. The secondary flow structure found by Hirota et al. (1992) was detected in rib-roughened channels with higher relative roughness (k/H) by Rau et al. (1998). They investigated the turbulent flow and heat transfer in a one- and a two-sided rib-roughened square channel for varying rib pitches ($6 \leq p/k \leq 12$, $k/H = 0.1$) at a Reynolds number of $Re_H = 3.0 \cdot 10^4$. Within the inter-rib spacing, the location of maximum heat transfer, vertical mean velocity, and velocity fluctuations coincided with the reattachment zones in inter-rib spacing center and in front of the rib. The effect of roughness parameters on the turbulent flow in a rib-roughened square channel with ribs ($p/k = 10$, $k/H = 0.1$, and $p/k = 6$, $k/H = 0.17$) applied on two opposite walls at a Reynolds number of $Re_H = 2.0 \cdot 10^4$ was investigated by Graham et al. (2004). The LDA measurements showed that the streamwise mean velocity at the channel center line varied sinusoidally in axial direction, which was reported earlier for rib-roughened circular pipes by Stukel et al. (1984). For the ribs with $p/k = 6$ and $k/H = 0.17$,

the flow field showed characteristics of a intermediate roughness flow laying between the d - and k -type roughness, which was found for turbulent boundary layer flows (Okamoto et al. 1993) and two-dimensional channel flows (Cui et al. 2003; Leonardi et al. 2003). It was shown that the peak Reynolds normal stresses and the friction factor increased with increasing relative roughness. A very extensive experimental study about the turbulent flow field in a one-sided rib-roughened channel with a high blockage ratio ($p/k = 10$, $k/H = 0.3$) at a Reynolds number of $Re_H = 4.0 \cdot 10^4$ was performed by Casarsa and Arts (2005). The presented particle image velocimetry (PIV) results complemented the heat transfer measurements by Cakan (2000). Overall, turbulence anisotropy dominated the entire flow field. Streamwise velocity fluctuations were the highest, and their peak values occurred above the rib crest and within the separated shear layer at the channel center plane. The PIV measurements of Wang et al. (2007) showed also a high degree of anisotropy. They measured the turbulent flow structures of separated flow in a channel with square ribs ($p/k = 12$, $k/H = 0.15$) applied on one wall at $Re_H = 2.2 \cdot 10^4$ by PIV. Results of instantaneous velocity fields revealed that spanwise vortices laid within the separated shear layer and the vorticity thickness grew linearly in streamwise direction. Longitudinal and lateral Taylor microscales derived from the corresponding auto-correlation profiles indicated that turbulence was far away from isotropic, and anisotropy increases with increasing distance from the wall. In a further PIV study for identical mean flow conditions, Wang et al. (2010) examined the flow structures in the vicinity of the rib ($p/k = 10$, $k/H = 0.2$). Their results showed that ejection events were the main contributor to the Reynolds shear stress at the rib leading edge, where the maximum Reynolds shear stress occurred. Cardwell et al. (2011) reported on turbulent flow structures in a two-sided oppositely rib-roughened square channel with square ribs ($p/k = 8$, $k/H = 0.12$) in a staggered configuration. From time-accurate flow field visualizations, unsteady burst events in the vicinity of the rib arguing the fluid mixing were identified. It was shown that two counter-rotating vortices were formed behind the rib producing a high-velocity jet in wall-normal direction, which displaced the shear layer flow toward the core flow, disrupted it, and caused a rapid fluid ejection into the core flow. The burst events occurred for all Reynolds numbers investigated ($Re_H = 2.5 \cdot 10^3$, $1.0 \cdot 10^4$, $2.0 \cdot 10^4$), but the burst frequency was Reynolds number dependent. Shear layer instabilities and the burst process resulted in the generation and shedding of coherent flow structures which can travel through the channel core before they diffuse. The unsteady turbulent flow field in a rib-roughened channel was also investigated by Coletti et al. (2013). They carried out PIV measurement in a square channel with square ribs

($p/k = 10$, $k/H = 0.1$) on one wall at a Reynolds number of $Re_H = 1.5 \cdot 10^4$. It was found that the separated shear layer flow was dominated by vortices which developed during the roll-up process of the shear layer formation around the rib leading and trailing edges. Coherent flow structures originated from the shear layer separation. The corresponding flow length scales differed in size and increased while moving downstream. Vortical as well as large-scale structures persisted along the entire inter-rib spacing while moving downstream and, thus, characterized the flow impingement on the successive rib where they participated again in the vortical flow structure generation and shedding. Fang et al. (2015) and Fang et al. (2017) investigated the turbulent flow around transverse and V-shaped ribs ($p/k = 8$, $k/H = 0.1$) in a square channel at Reynolds numbers of $1.08 \cdot 10^4 \leq Re_{D_h} \leq 1.36 \cdot 10^4$ by means of PIV and large eddy simulation. Their analysis for the transverse ribs revealed that the anisotropic flow field at the rib-roughened wall was governed by swirling flow motion. Above the rib crest, streamwise-elongated flow structures developed, while none of them appeared below the rib height within the inter-rib spacing due to the geometric constraints. The *TKE* distribution was dominated by the streamwise Reynolds normal stress, and the streamwise-wall-normal Reynolds shear stress and the peaks coincided with large primary mean shear above the rib crest. Mahmoodi-Jezeh and Wang (2020) reported very interesting results about the unsteady flow physics near the rib. They investigated the effect of the rib-height-to-channel-height ratio ($k/H = 0.05, 0.1, 0.2$) on the turbulent flow field at a Reynolds number of $Re_H = 5.6 \cdot 10^3$ by means of direct numerical simulation (DNS). Similar to the two-dimensional case reported by Ikeda and Durbin (2007), the presence of the ribs caused a non-equilibrium between turbulence production and dissipation to develop in a layer above the ribs. The dominant source term of the *TKE* budget was the production term with a maximum immediately above the rib crest. In contrast to smooth channel flows, the turbulent diffusion term and the convection term contributed remarkably to the *TKE*.

Although turbulent flows in rib-roughened square channels were frequently investigated, the literature reporting detailed measured high-order statistical moments for Reynolds number flows relevant for thermally highly loaded heat exchanger components ($Re_H \gtrsim 5.0 \cdot 10^4$) is somewhat rare. Questions regarding turbulent flow physics and transport mechanisms at different regions of the flow field remain unanswered. The present study aims at an extensive analysis of the complex turbulent flow in a one-sided rib-roughened square channel at Reynolds numbers of $Re_H = 5.0 \cdot 10^4$ and $1.0 \cdot 10^5$. LDA measurements of the velocity in the fully developed flow regime were carried out to provide one-point statistics. Mean velocity, second-order statistical moments

as well as *TKE* contributors were determined. The obtained results enable the identification of regions with high turbulent mixing, explanation of transport phenomena and the validation of computational methods and turbulence models.

2 Experimental facility

The experiments were performed in a closed air loop test facility as schematically depicted in Fig. 1a. It consisted of the test section with an upstream installed entrance channel, a 3" piping system, four frequency-controlled side channel blowers, four water-cooled heat exchangers, exhaust and safety valves, a cyclone separator, flow conditioning devices, as well as mass flow and thermal measurement devices.

The air flow was provided by four side channel blowers, which were PID-controlled by a customized LabView software with the Reynolds number $Re_H = \dot{m} \cdot H^{-1} \cdot \mu(T_{in})^{-1}$ as the control variable. The mass flow rate \dot{m} was measured by a Coriolis flow meter, while the dynamic viscosity μ for air was approximated from the measured inlet fluid temperature T_{in} by a fourth-order polynomial (VDI 2010). Temperature-controlled water-cooled heat exchangers downstream the blowers facilitated nearly constant air temperatures during the tests. The inlet pressure p_{in} and the inlet fluid temperature T_{in} were measured upstream the main test section. The test facility was operated under isothermal conditions. The operating pressure (= inlet pressure p_{in}) was adjusted manually by a control valve leveling the pressure increase by the overpressure injection of the Di-Ethyl-Hexyl-Sebacat

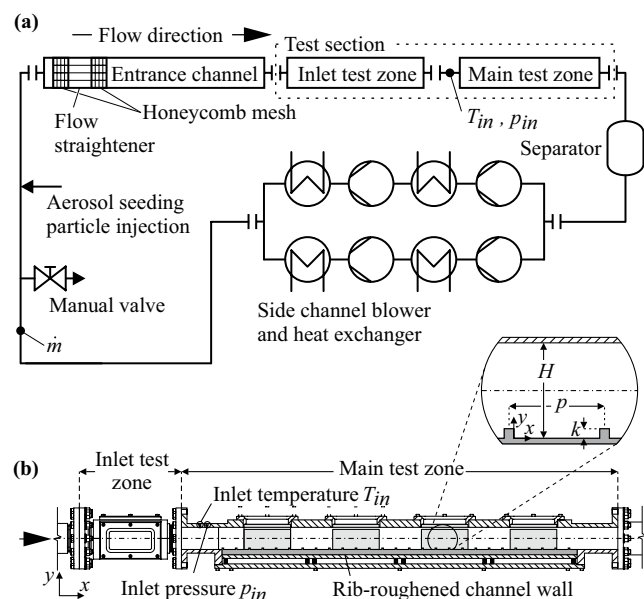


Fig. 1 a Piping diagram of the air loop test facility and b sketch of the test section and nomenclature of the rib configuration

aerosol seeding particles for the LDA measurements. Two transition pieces transferred the circular cross section of the piping system to the $60 \cdot 60 \text{ mm}^2$ square section cross of the entrance channel and of the test section. The length of the entrance channel was 3056 mm, and the length of the test section was 1180 mm. A flow straightener and two honey comb meshes for minimizing swirl effects were inserted at the entrance channel inlet. Immediately behind the downstream located honeycomb mesh, the air flow was tripped by a peripherally installed thin wire with a diameter of 1.2 mm to speed up the turbulent flow development. The test section is shown in Fig. 1b. It contained an inlet test zone and the main test zone. While the inlet test zone was smooth, the bottom wall of the main test zone was periodically structured by ribs with a $4.0 \cdot 4.0 \text{ mm}^2$ square cross section and a pitch between the ribs of 36 mm. The pitch was large enough to reproduce the flow pattern of the k -type roughness at the channel center plane as known for flows in square channels of Reynolds numbers of $O(10^4)$ (Cardwell et al. 2011). The channel bottom and the ribs were made of black polyamide. The surface was fine grinded resulting to an arithmetically averaged surface roughness of $Ra = 1.0 \mu\text{m}$. Both test zones contained windows of homogenous silica Spectrosil glass at the side walls and at the top providing optical accessibility for the LDA measurements.

3 Instrumentation

Single and two-component velocities were measured with a Dantec Dynamics fiber optical LDA system operating in the backscatter mode. Two blue beams of 488 nm wavelength and two green beams of 514.5 nm wavelength were provided by a Spectra-Physics air-cooled 320 mW Ar-Ion Laser with a Bragg cell for the frequency shift. A two-component 60 mm FiberFlow LDA probe with a 160 mm focal length lens was used for measuring the velocities in streamwise and wall-normal direction. The measurement volume diameter and length of the two-component probe were $78 \mu\text{m}$ and $658 \mu\text{m}$ for the streamwise velocity component (u) and $74 \mu\text{m}$ and $625 \mu\text{m}$ for the wall-normal velocity component (v). Signals were processed by using a Burst Signal Analyser Flowmaster P80. The flow was seeded by aerosol particles which were generated from Di-Ethyl-Hexyl-Sebacat fluid by a Topas ATM 210/H. The particles were injected with overpressure into the test facility upstream the flow conditioner. The mean particle size ranged from 0.15 to $0.2 \mu\text{m}$, so that turbulent fluctuations up to several thousand Hz were expected to be captured by LDA (Ruck 1990). The two-component LDA probe was mounted beside the test section on a three-axis Newport traverse system. The spatial accuracy of the traverse system was $\pm 10 \mu\text{m}$. By means of the BSA Flow Software 6.5, the LDA measuring process and the traverse

system were controlled, and the recorded velocity data were transferred. For each velocity measurement run at one measurement location, the inlet pressure p_{in} , the inlet temperature T_{in} , and the mass flow rate \dot{m} were time-averaged over the LDA acquisition time and additionally recorded. LDA measurements were carried out for Reynolds numbers of $Re_H = 5.0 \cdot 10^4$ and $1.0 \cdot 10^5$. The sample number per measurement point depended on the wall distance. Measurements contained a minimum of 50,000 samples very close to the rib-roughened channel wall and 200,000 samples within the near-wall region and the channel core region for all Reynolds numbers. The data rate varied with the wall distance and Reynolds number in the range of hundred samples s^{-1} in the near-wall region up to 3000 samples s^{-1} in the channel core region. The wall-closest measurement point where burst signals were detected was set to a wall distance of 0.08 mm due to the measurement volume configuration. The experimental setup enabled measurements of the vertical velocity only for $y/k > 1$ in the region $0.1 \geq x/k \geq 7.9$. Velocities were measured in the burst acquisition mode. Residence time weighting (George et al. 1978) was applied for the time-averaging in the calculation of the first absolute and high-order central moments of the velocity.

All measurements were taken under global steady-state conditions. The averaged inflow turbulence intensity $I = \sqrt{1/2 \cdot (\langle u'^2 \rangle + \langle v'^2 \rangle)} / \sqrt{(\langle u \rangle^2 + \langle v \rangle^2)}$ at the channel center line in the smooth inlet test zone was 4.8% and 5.0% for $Re_H = 5.0 \cdot 10^4$ and $1.0 \cdot 10^5$, respectively. The symbol $\langle \rangle$ stands for the time-averaged mean and the symbol $'$ labels the fluctuation of the instantaneous value about its mean, e. g., $u' = u - \langle u \rangle$. The normalized streamwise mean velocity $\langle u \rangle$ and the standard deviation of the streamwise velocity $\sqrt{\langle u'^2 \rangle}$ of the turbulent developed inlet flow over the wall-normal direction at the smooth inlet region of the test section are shown in Fig. 2. LDA measurements were made systematically between the 17th and 18th ribs along the channel center plane which spanned in streamwise (x) and wall-normal (y) direction at spanwise location of $z/e = 0$. The origin of the Cartesian coordinate system (x, y, z) for the analysis was located at the leeward surface of the 17th rib and the channel bottom wall (Fig. 1b). Flow field periodicity and the fully developed flow are crucial requirements to confirm negligible effects of the inlet and outlet boundary conditions on the measured flow field. Both conditions were verified by comparing the mean velocities and Reynolds stresses which were measured at the same relative position within two subsequent measurement regions displaced by a streamwise offset of one rib pitch. Figure 3 shows distributions of the streamwise mean velocity and the standard deviation of the streamwise velocity normalized by the bulk velocity $u_B = \langle \dot{m} \cdot \rho \langle T_{in}, p_{in} \rangle \rangle^{-1} \cdot H^{-2}$ over the wall-normal direction at a streamwise position of $x/k = -0.5$ or 8.5 and 3.0 or 12.0 for a Reynolds number of $Re_H = 1.0 \cdot 10^5$. The

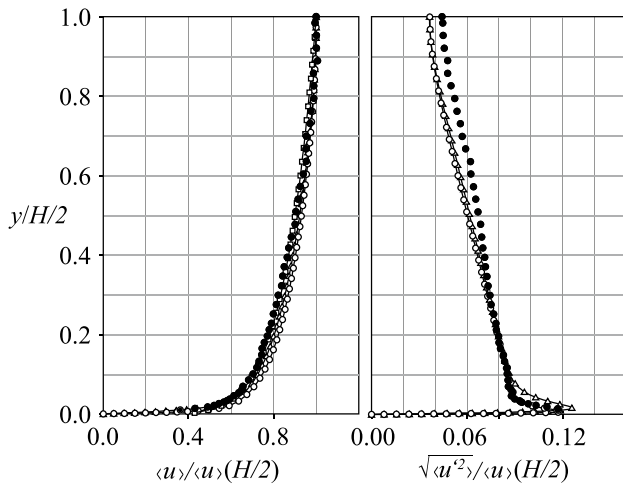


Fig. 2 Normalized “filledcircle” mean streamwise velocity and “smallfilled circle” standard deviation of the streamwise velocity measured at the smooth inlet region of the test section for $Re_H = 1.0 \cdot 10^5$ ($Re_\tau = 0.5 \cdot c_f^{1/2} \cdot 2^{-1/2} \cdot u_B \cdot H \cdot \nu(T_{in})^{-1} \approx 1300$, with the kinematic viscosity for air (VDI 2010) and the friction factor determined from the correlation of Petukhov (1970)) for smooth channels, compared with the “diamond” 1/7 power-law and DNS results for a turbulent channel flow at “blacktriangle” $Re_\tau = 950$ and “opencircle” $Re_\tau = 2000$ from Hoyas and Jiménez (2006). Mean uncertainty in $\langle u \rangle / \langle u \rangle (y = H/2) : \pm 0.0038$ and in $\sqrt{\langle u'^2 \rangle} / \langle u \rangle (y = H/2) : \pm 0.0028$

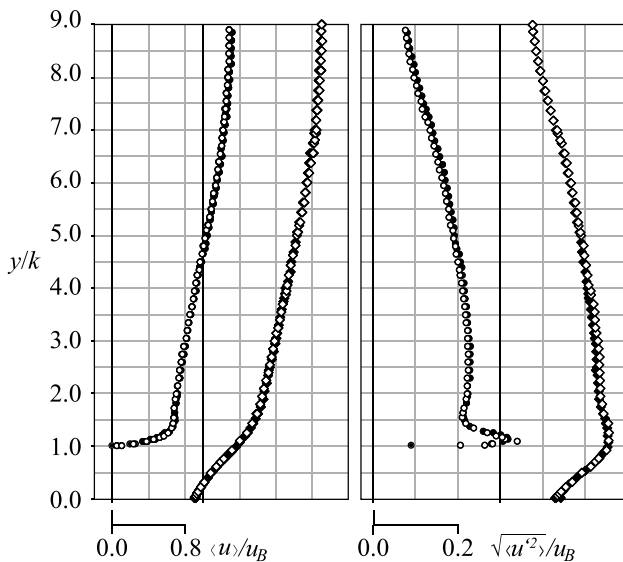


Fig. 3 Normalized mean streamwise velocity and standard deviation of streamwise velocity measured at the same relative streamwise positions between the 17th and 18th and the 18th and 19th ribs for $Re_H = 1.0 \cdot 10^5$: “opencircle” $x/k = -0.5$, “filledcircle” $x/k = 8.5$, “diamond” $x/k = 3.0$ and “blackdiamond” $x/k = 12.0$. Mean uncertainty in $\langle u \rangle / u_B : \pm 0.0240$ and in $\sqrt{\langle u'^2 \rangle} / u_B : \pm 0.0177$

distributions determined at the same relative streamwise position were almost congruent confirming the flow field periodicity and the fully developed flow assumption in the measurement region.

4 Measurement uncertainty estimates

Measurement uncertainties were determined as described by Kline and McClintock (1953). The stochastic uncertainty estimates based on the 95% confidence levels and were calculated from $\pm 1.96 \cdot \sqrt{\text{var}\{q\}}/N$, with the sampling variances $\text{var}\{ \}$ of the measured variable q and the number of samples N (Nobach and Tropea 2007). The variances were calculated under the assumption of normally distributed samples. The maximum uncertainty of the reattachment length was $\pm 0.125 \cdot k$ and of the Reynolds number was $\pm 2700, \pm 3200$ and ± 4200 at $Re_H = 5.0 \cdot 10^4, 1.0 \cdot 10^5$ and $1.5 \cdot 10^5$. For evaluating the stochastic uncertainty of the mean velocity and Reynolds stresses, the sampling variances were determined by estimators given in Benedict and Gould (1996), in which the residence time weighting (George et al. 1978) was applied for calculating the high-order moments. The variance was estimated at each measurement location for the mean velocities and the Reynolds stresses. Statistically independent samples were expected to be recorded after two integral time scales $2 \cdot t_{int}$ (Tennekes and Lumley 1972) which were calculated from integrating the normalized temporal autocorrelation function up to the first zero-crossing. In this case, $N = t/2 \cdot t_{int}$ is the number of statistically independent samples in the confidence level estimator, with the sampling time at each location t . The mean uncertainty estimates for the statistical moments of the velocity normalized by the bulk velocity are given in the figure captions.

5 Results

The results presented Figs. 2 to 13 were normalized with the bulk velocity u_B and the channel height H or the rib height k . For the sake of clarity, only 40–50% of the measurement points were plotted, and the presented velocity plots were smoothed by a moving mean, i.e., each value for a specified location was averaged over a sliding window of three values centered at the value itself. The measured and smoothed values were almost congruent and averaging effects on the high gradient regions were negligible as shown exemplary in Fig 4. Features of the mean flow field were sketched additionally in the plots. The location of the separated shear layer boundaries (dashed lines) was approximated from the local maxima of the wall-normal $\langle u'^2 \rangle$ gradients. It is mentioned that the sketched flow patterns are rough estimates of the

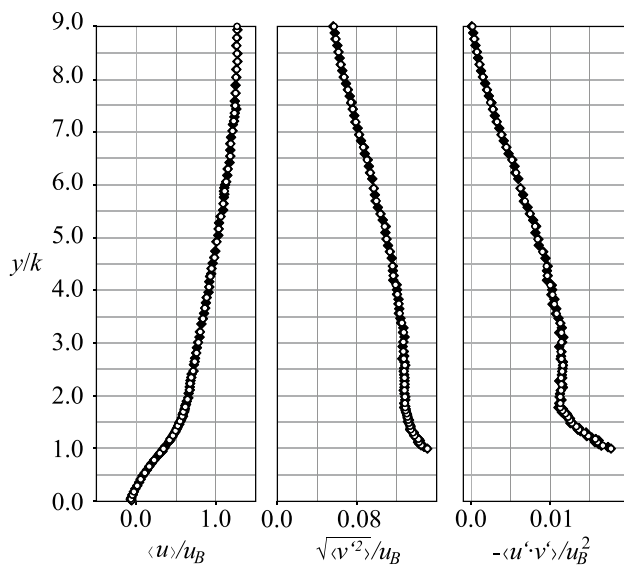


Fig. 4 Normalized mean streamwise velocity $\langle u \rangle$, standard deviation of the wall-normal velocity $\sqrt{\langle v'^2 \rangle}$ and Reynolds shear stress $-\langle u' \cdot v' \rangle$ at $x/k = 3.0$ for $Re_H = 5.0 \cdot 10^4$: “open circle” smoothed by moving average and “black diamond” measured data set. Mean uncertainty in $\langle u \rangle / u_B : \pm 0.0090$, in $\sqrt{\langle v'^2 \rangle} / u_B : \pm 0.0011$ and in $-\langle u' \cdot v' \rangle / u_B^2 : \pm 0.0009$

layout and size of the mean flow pattern and should only be used for a better interpretation of the measurement results.

5.1 Reynolds number dependency

Former studies showed that mean velocities and Reynolds stresses exhibit a Reynolds number insensitivity in two-dimensional rough-wall flows. For the turbulent channel flow with one rib-roughened wall, Hanjalić and Launder (1972) showed that the Reynolds number dependency of high-order statistical moments in the near rough-wall region vanished when they were normalized by the rough-wall friction velocity. Bandyopadhyay (1987) suggested a Reynolds independency of the roughness function, which was verified by Leonardi et al. (2003). For turbulent flow over a rib-roughened plate, Okamoto et al. (1993) found that the Reynolds number effect on the optimum rib pitch for maximum turbulence intensity seems to be insignificant. Cui et al. (2003) compared the mean flow velocities in a periodic channel with those of the rough-wall boundary layer flow described by Okamoto et al. (1993) and suggested a slight Reynolds number effect on the mean velocity profile as well as a Reynolds number dependency of the location of the demarcation line between the inner roughness layer and the outer flow. Although turbulent flow in rib-roughened square channel was investigated in the past, studies reporting about the Reynolds number dependency of the flow field are rare. Cardwell et al. (2011) have shown that the mean velocities

and *TKE* distributions of the fully developed flow in a one-sided rib-roughened channel were almost Reynolds-number-insensitive for Reynolds numbers of $1.0 \cdot 10^4$ and $2.0 \cdot 10^4$. In the present case, the resolved rib-roughened near-wall region was governed by rib-induced flow structures. Since viscous effects were almost negligible when compared to the turbulent and convective momentum transport, the bulk velocity u_B and the channel height H or rib height k were used for the normalization of the velocity distributions instead of the viscous inner scale and the friction velocity. The normalized distributions of mean velocity (Figs. 5, 6) and second-order statistical moments (Figs. 8, 9, 10, 11) showed similar trends for the Reynolds numbers of $Re_H = 5.0 \cdot 10^4$ and $1.0 \cdot 10^5$. As shown later in detail (Fig. 13), the same turbulent transport mechanism was identified for both Reynolds numbers. Nevertheless, a small Reynolds number dependency can be inferred from the results, especially in the inter-rib spacing between $x/k = 2.0$ and 6.0 . It was found that the recirculation region elongated with the Reynolds number (Fig. 7). Differences between the wall-normal distributions of the first- and high-order statistical moments at different streamwise positions were restricted to a layer of nearly the same height above the ribs. The height of the layer depended on the statistical moment and was about one rib height narrower within the inter-rib spacing than in the vicinity of the rib. Outside the layer, the distributions in wall-normal direction were independent of the streamwise position and Reynolds number.

5.2 Time-averaged streamwise and wall-normal velocity

Distributions of the mean velocities in streamwise and wall-normal direction along the center plane are displayed in Figs. 5 and 6. For both Reynolds numbers, the time-averaged velocity profiles show the same trends. The flow field was significantly affected by the ribs. Its three-dimensionality is reflected in the downwards directed wall-normal mean velocity within the entire upper channel half, which was attributed to the secondary flow motion of a counter-rotating pair of large streamwise-elongated vortices (Hirota et al. 1992; Rau et al. 1998). The increased wall flow resistance at the rib-roughened wall shifted the fluid toward the opposite smooth channel wall which was consistent with the findings by Fang et al. (2017) who reported for the turbulent flow at $Re_H = 1.0 \cdot 10^4$ that high levels of streamwise momentum were concentrated at the upper channel half. Above $y/k = 5$, the mean streamwise velocity distributions and above $y/k = 6$, the mean wall-normal velocity distributions were independent of the streamwise position.

The velocity distributions of the three-dimensional flow field reflected well-known flow field characteristics of the k -type roughness near the rib-roughened channel wall

Fig. 5 Normalized mean streamwise velocity $\langle u \rangle$ distributed in the wall-normal direction at different streamwise positions: “Diamond” $Re_H = 5.0 \cdot 10^4$ and “filled-circle” $Re_H = 1.0 \cdot 10^5$. Mean uncertainty in $\langle u \rangle / u_B : \pm 0.0161$ and ± 0.0189 for $Re_H = 5.0 \cdot 10^4$ and $1.0 \cdot 10^5$

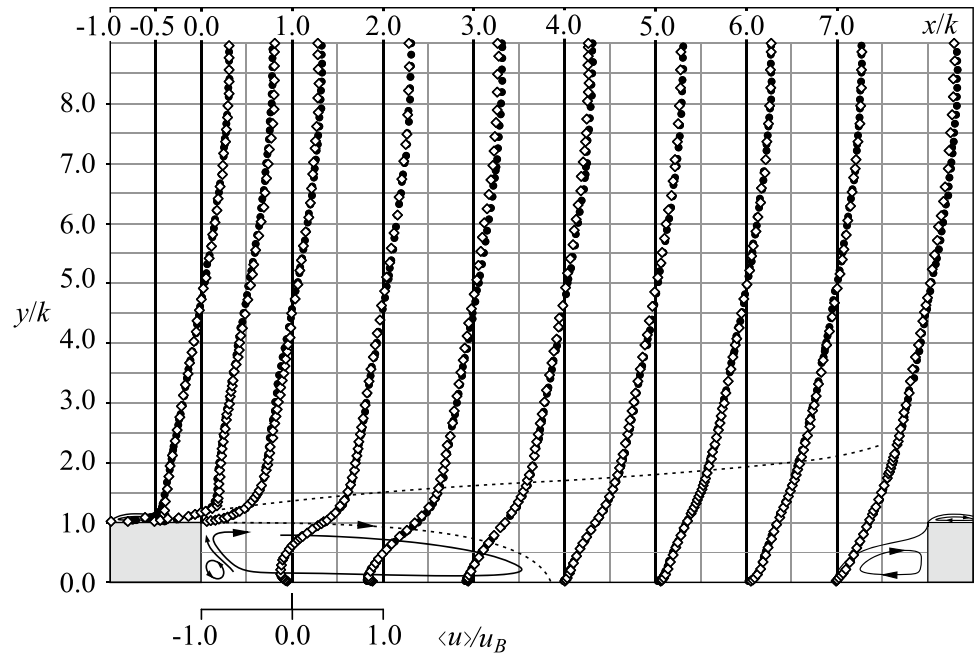
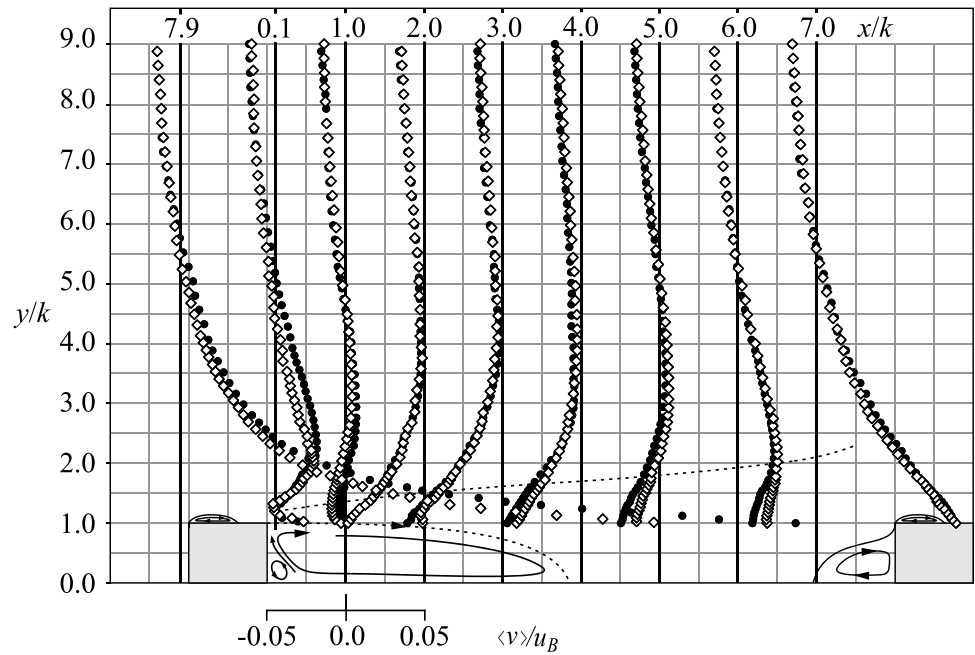


Fig. 6 Normalized mean wall-normal velocity $\langle v \rangle$ distributed in the wall-normal direction at different streamwise positions: “Diamond” $Re_H = 5.0 \cdot 10^4$ and “filled-circle” $Re_H = 1.0 \cdot 10^5$. Mean uncertainty in $\langle v \rangle / u_B : \pm 0.0023$ and ± 0.0022 for $Re_H = 5.0 \cdot 10^4$ and $1.0 \cdot 10^5$



region. The flow was accelerated near the windward rib surface due to the upward flow deflection by rib blockage, causing a steep rise of the mean velocities above the rib. The maximum mean wall-normal velocity in upward direction at the rib leading edge was $0.71 \cdot u_B$ for $Re_H = 5.0 \cdot 10^4$ and $0.79 \cdot u_B$ for $Re_H = 1.0 \cdot 10^5$. A very small region of negative mean streamwise velocity close to the rib crest at $x/k = -0.5$ indicated the tail end of the small recirculation bubble which was formed by flow detachment at the rib leading edge due to the large pressure gradient between the windward rib surface and the rib crest (Leonardi et al. 2003). The strong flow

acceleration caused an intense attached shear layer downstream the recirculation bubble that separates at the rib trailing edge. The sudden cross-section expansion of the channel behind the rib deflected the fluid toward the channel bottom wall. The negative mean streamwise velocity at $x/k = 1.0, 2.0,$ and 3.0 close to the channel bottom wall referred to the reversed fluid motion of the clockwise rotating spacious recirculation vortex which was entrapped between the leeward rib surface, channel bottom wall, and the separated shear layer as reported by Labbé (2013) who investigated the turbulent flow field in a one-sided rib-roughened square

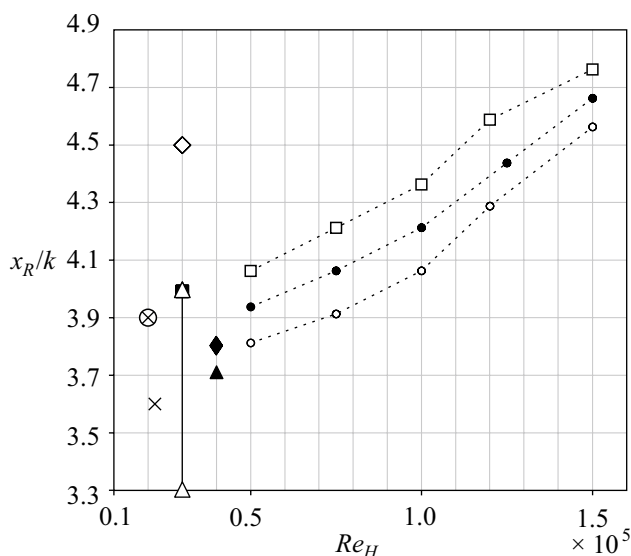
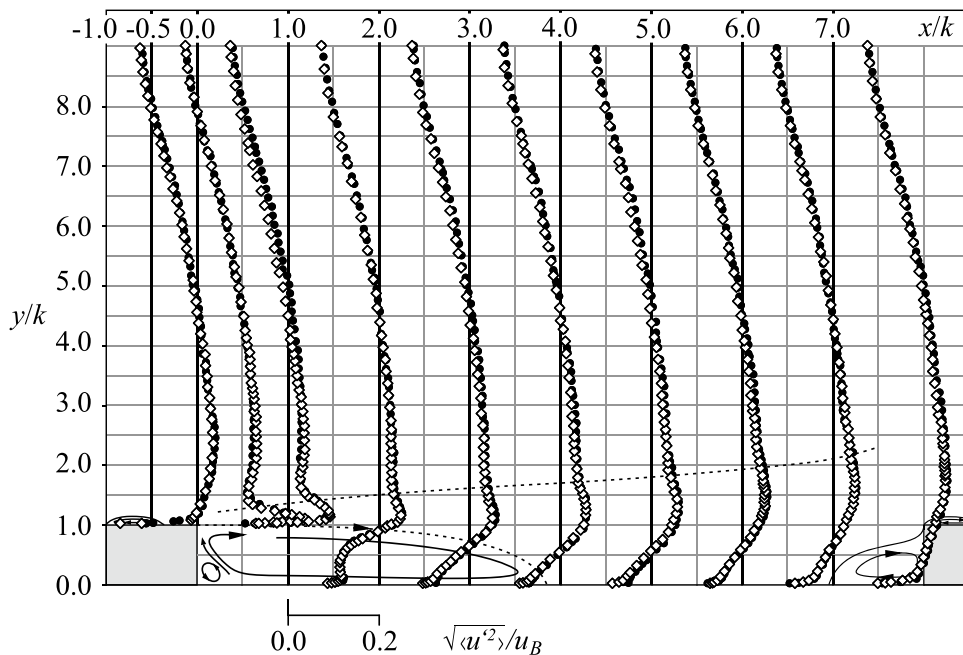


Fig. 7 Normalized reattachment length $x_R k$ versus Reynolds numbers Re_H . LDV measurements at “filledcircle” $y/k = 0.02$ and “open-circle” $y/k = 0.04$ and linearly extrapolated to “square” $y/k = 0.00$. “triangle” Rau et al. (1998), $6 \leq p/k \leq 16$, $k/H = 0.1$. “cross” Cui et al. (2003), $p/k = 10$, $k/H = 0.1$. “blacksquare” Sewall and Tafti (2004), $p/k = 10$, $k/H = 0.1$. “Diamond” Ahn et al. (2005); $p/k = 10$, $k/H = 0.3$. “blackdiamond” Casarsa and Arts (2005), $p/k = 10$, $k/H = 0.3$. “cross” Wang et al. (2007), $p/k = 10$, $k/H = 0.15$. “blacktriangle” Labbé (2013), $p/k = 10$, $k/H = 0.3$

rib surface, the reverse flow was directed upwards to the rib trailing edge yielding a local peak of positive mean vertical velocity between $y/k = 1.0$ and $y/k = 1.17$ at $x/k = 0.1$. The adverse pressure gradient caused a downward flow motion behind the rib, and thus, the positive mean wall-normal velocities reduced further downstream. Minimum mean wall-normal velocities occurred beneath $y/k = 1.0$ between $x/k = 2.0$ and 4.0 . Due to the downwash, the separated shear layer reattached at the channel bottom wall within the inter-rib spacing. The reattachment was already completed at $x/k = 4.0$ for $Re_H = 5.0 \cdot 10^4$, whereas a negative mean streamwise velocity immediately above the channel bottom wall at $x/k = 4.0$ for $Re_H = 1.0 \cdot 10^5$ suggested the reattachment to occur a bit further downstream. The accompanied increasing elongation of the large recirculation region in streamwise direction with the Reynolds number region was reflected in deviations of the mean wall-normal velocity profiles between $x/k = 3.0$ and 6.0 . A new boundary layer developed in the post-reattachment region ($x/k = 5.0, 6.0$) against an adverse pressure gradient which was indicated by the dips of the velocity profiles downstream of the reattachment and was consistent with the PIV results found by Wang et al. (2007). The flow detached in front of the subsequent rib forming vortical structures with reversed flow which were indicated by the small amount of negative mean streamwise velocities close to the channel bottom at

Fig. 8 Normalized standard deviation of the streamwise velocity $\sqrt{\langle u'^2 \rangle}$ distributed in the wall-normal direction at different streamwise positions: “Diamond” $Re_H = 5.0 \cdot 10^4$ and “smallfilled circle” $Re_H = 1.0 \cdot 10^5$. Mean uncertainty in $\sqrt{\langle u'^2 \rangle}/u_B : \pm 0.0115$ and ± 0.0134 for $Re_H = 5.0 \cdot 10^4$ and $1.0 \cdot 10^5$



channel with a 450% higher relative roughness (compared to the present case) at a Reynolds number of $Re_H = 4.0 \cdot 10^4$. The maximum negative mean streamwise velocity was about -0.12 to $-0.13 \cdot u_B$ at $x/k = 1.0$ and -0.06 to $-0.1 \cdot u_B$ at $x/k = 3.0$ for both Reynolds numbers. Close to the leeward

$x/k = 7.0$. The increase in the mean wall-normal velocities reflected the proximity to the subsequent rib. The rib blockage caused an upward flow motion at $x/k = 6.0, 7.0$ and 7.9 ,

Fig. 9 Normalized standard deviation of the wall-normal velocity $\sqrt{\langle v'^2 \rangle}$ distributed in the wall-normal direction at different streamwise positions: “Diamond” $Re_H = 5.0 \cdot 10^4$ and “smallfilled circle” $Re_H = 1.0 \cdot 10^5$. Mean uncertainty in $\sqrt{\langle v'^2 \rangle}/u_B$: ± 0.0019 and ± 0.0018 for $Re_H = 5.0 \cdot 10^4$ and $1.0 \cdot 10^5$

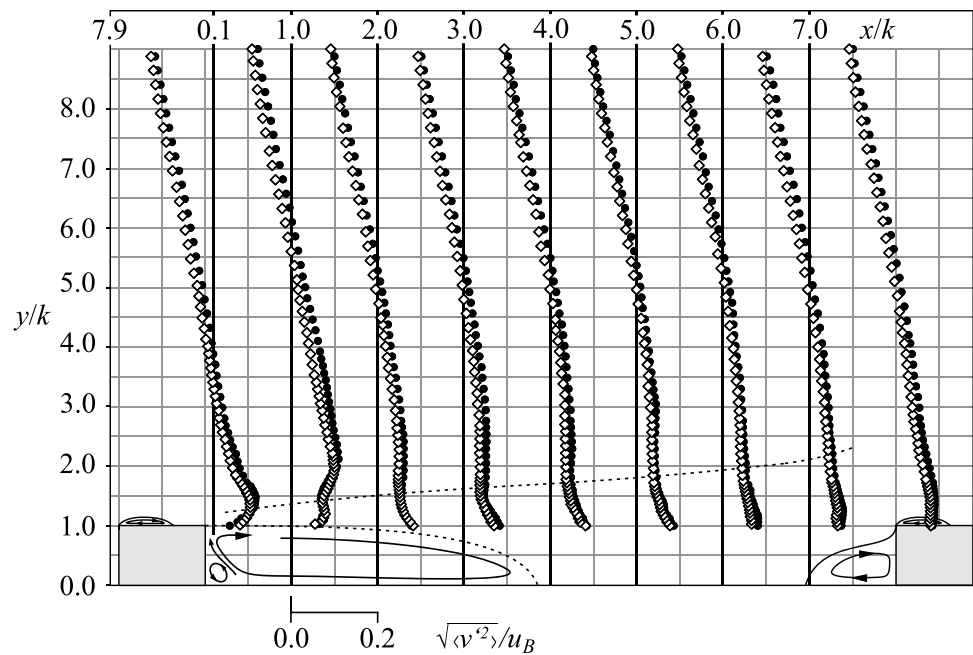
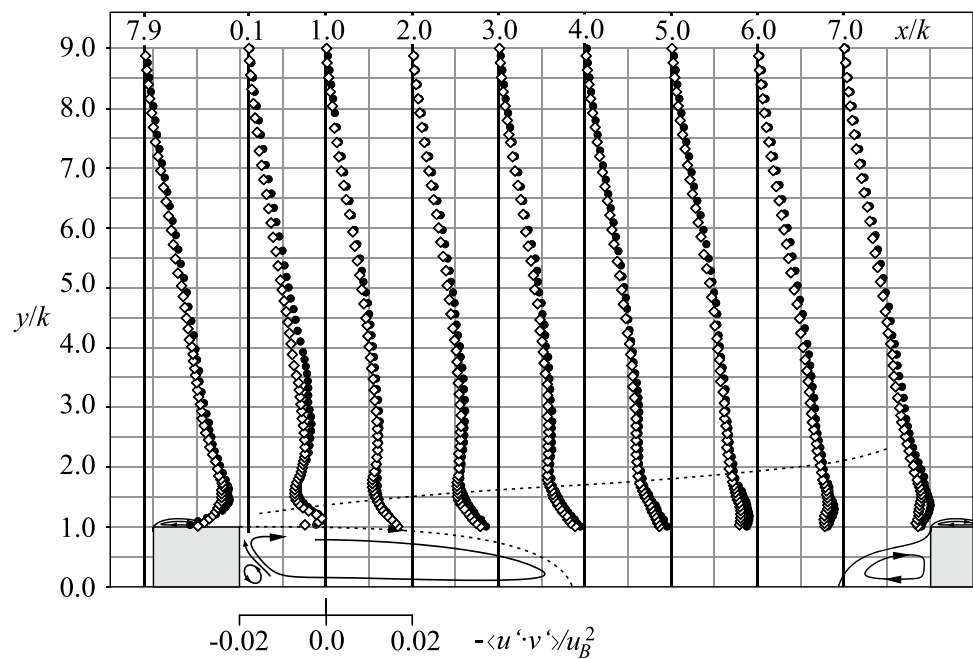


Fig. 10 Normalized Reynolds shear stress $-\langle u' \cdot v' \rangle$ distributed in the wall-normal direction at different streamwise positions: “Diamond” $Re_H = 5.0 \cdot 10^4$ and “small-filled circle” $Re_H = 1.0 \cdot 10^5$. Mean uncertainty in $-\langle u' \cdot v' \rangle/u_B^2$: ± 0.0017 and ± 0.0016 for $Re_H = 5.0 \cdot 10^4$ and $1.0 \cdot 10^5$



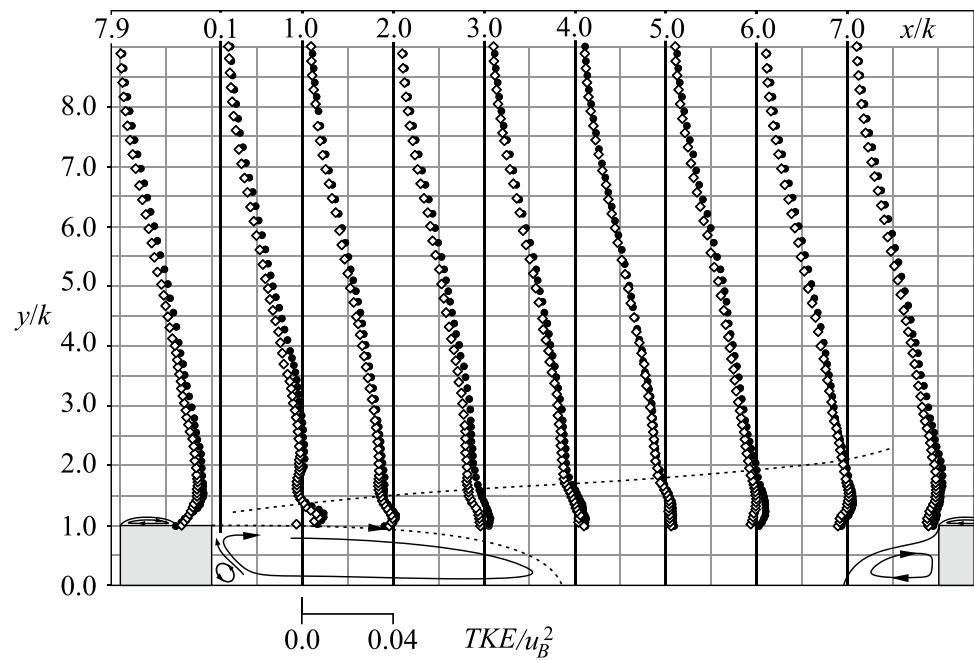
which streamed against the downwards directed mean flow driven by the secondary flow motion (Hirota et al. 1992).

5.3 Reattachment length

The distinction of the mean streamwise velocities close to the channel bottom at $x/k = 4.0$ (Fig. 5) and of the mean wall-normal velocities around $y/k = 1.0$ at $x/k = 4.0, 5.0$ and 6.0 (Fig. 6) for $Re_H = 5.0 \cdot 10^4$ and $1.0 \cdot 10^5$ suggested a Reynolds number dependency of the mean flow pattern.

The time-averaged streamwise length of the large recirculation region behind the rib is indicated by the time-averaged location of the shear layer reattachment-issued saddle point (Wang et al. 2010). The reattachment length x_R , namely the distance from the leeward rib surface to the reattachment point, corresponds to the location where the mean streamwise velocity immediately above the channel wall switched its sign from negative to positive (and so would the wall shear stress do). It depends on the rib pitch for boundary layer flows (Okamoto et al. 1993) and

Fig. 11 Normalized turbulence kinetic energy TKE distributed in the wall-normal direction at different streamwise positions: “Diamond” $Re_H = 5.0 \cdot 10^4$ and “smallfilled circle” $Re_H = 1.0 \cdot 10^5$. Mean uncertainty in TKE/u_B^2 : ± 0.0190 and ± 0.0168 for $Re_H = 5.0 \cdot 10^4$ and $1.0 \cdot 10^5$



internal duct flows (Rau et al. 1998). Figure 7 shows the reattachment length, determined from velocity measurements very close to the channel bottom wall at $y/k = 0.02$ and 0.04 , as a function of the Reynolds number. The determined lengths were within ranges typically known from turbulent flow in rib-roughened square channels at lower Reynolds numbers. The determination method was found to be sensitive to the wall-normal location of the streamwise velocity measurement: the larger the wall distance of the measurement location, the smaller the reattachment length. As expected from the mean streamwise velocity distributions, the reattachment length decreased with increasing wall distance of the streamwise velocity measurement location due to the wall-normal reduction of the tail end of the recirculation region. Depending on the measurement location at $y/k = 0.02$ and 0.04 , the reattachment length increased from $x_R/k = 3.9$ at $Re_H = 5.0 \cdot 10^4$ to $x_R/k = 4.6$ at $Re_H = 1.5 \cdot 10^5$ and from $x_R/k = 3.8$ at $Re_H = 5.0 \cdot 10^4$ to $x_R/k = 4.6$ at $Re_H = 1.5 \cdot 10^5$, respectively. By means of a linear extrapolation, the reattachment length on the channel bottom wall was determined. As shown in Fig. 7, it increased from $x_R/k = 4.1$ at $Re_H = 5.0 \cdot 10^4$ to $x_R/k = 4.9$ at $Re_H = 1.5 \cdot 10^5$. In contrast to lower Reynolds number flows (Islam et al. 2002), the reattachment length was sensitive to the Reynolds number. Considering the reduced upward velocity at $x/k = 5.0$ and 6.0 in Fig. 6, it was apparent that an increased elongation of the recirculation region caused the increase in the reattachment length for increasing Reynolds numbers. It is supposed that the deviations of the statistical moments in the investigated Reynolds number range based possibly on the minor elongation increase in the

recirculation region. On the assumption that the elongation grows continuously for increasing Reynolds numbers, it can be speculated that the recirculation region covers the entire inter-rib spacing for very high Reynolds numbers and, thus, an intermediate or d -type roughness (Perry et al. 1969) like flow field along the channel center plane would occur for relatively large rib-height-to-rib-pitch ratios.

5.4 Reynolds normal and shear stresses

Distributions of the normalized standard deviation of the streamwise velocity $\sqrt{\langle u'^2 \rangle}$ and of the wall-normal velocity $\sqrt{\langle v'^2 \rangle}$ along the center plane at Reynolds numbers of $Re_H = 5.0 \cdot 10^4$ and $1.0 \cdot 10^5$ are displayed in Figs. 8 and 9. The corresponding Reynolds shear stress distributions $-\langle u' \cdot v' \rangle$ are shown in Fig. 10. For both Reynolds numbers, the respective distributions are nearly congruent. The slight Reynolds number dependency can be inferred from the Reynolds shear stress distributions around $y/k = 1.0$ in the post-reattachment region where the mean wall-normal velocities showed the largest deviation. The Reynolds stresses were significantly enhanced by the ribs throughout the resolved channel region reflecting the intensified mixing between the near-wall flow and the channel core flow, which has been also noted previously for flow of lower Reynolds numbers in rib-roughened two-dimensional and squared channels. The streamwise Reynolds normal stress was the highest, which was consistent with the PIV results by Casarsa and Arts (2005). The Reynolds shear stress converged to zero at $y/k = 9$. Since $-\langle u' \cdot v' \rangle$ originates in ejection and sweep events (e.g., Wallace 2016), a deep

penetration of rib-induced turbulent transport into the core flow can be supposed from the present results.

The strong shear layer above the rib resulted in a high Reynolds stress production. In accordance with the DNS results found by Mahmoodi-Jezeh and Wang (2020), the maximum streamwise Reynolds normal stress $\langle u'^2 \rangle$ occurred at the rib crest as shown in Fig. 8. Close to the rib crest at $x/k = -0.5$ and $y/k = 1.1$, the maximum streamwise velocity fluctuation was $\sqrt{\langle u'^2 \rangle}/u_B = 0.34$ and 0.32 for $Re_H = 5.0 \cdot 10^4$ and $1.0 \cdot 10^5$, respectively. Peaks of $\sqrt{\langle u'^2 \rangle}/u_B$ varied between 0.25 and 0.27 in the inter-rib spacing. Between $x/k = 1.0$ and 3.0 , the wall-normal location of $\sqrt{\langle u'^2 \rangle}$ peaks increased slightly from $y/k = 1.16$ to 1.25 . The peak locations laid above the location of the inflection points of the mean streamwise velocity distribution ($\partial^2 \langle u \rangle / \partial y^2 = 0$). The different wall-normal locations of $\sqrt{\langle u'^2 \rangle}$ peaks and $\partial^2 \langle u \rangle / \partial y^2 = 0$ were assumed to be caused by diffusional transport. The wall-bounded shear layer of the reversed flow close to the channel bottom wall in the recirculation region at $x/k = 1.0$ caused a local $\sqrt{\langle u'^2 \rangle}$ maximum. For $Re_H = 1.0 \cdot 10^5$, the local maximum persisted in the recirculation region further downstream and decreased from $\sqrt{\langle u'^2 \rangle}/u_B = 0.12$ at $x/k = 1.0$ and $y/k = 0.11$ toward the shear layer reattachment point. In the post-reattachment region ($x/k \geq 4$), $\sqrt{\langle u'^2 \rangle}$ peaks drifted away from the wall in streamwise direction with an inclination angle of ~ 20 deg as shown in Fig. 8. It correlated with the linear shear layer thickness growth in streamwise direction reported by Wang et al. (2007) and the height increase in the shear layer reported by Cardwell et al. (2011). The fluid acceleration in the proximity of the windward rib surface caused high mean shear rates in the velocity field which resulted in a Reynolds stress enhancement as depicted for all measured Reynolds stresses at $x/k = -1.0$ and 7.9 . The distributions of $\sqrt{\langle u'^2 \rangle}$ in Fig. 8 and $-\langle u' \cdot v' \rangle$ in Fig. 10 showed similar trends within the separated shear layer behind the rib. In accordance with Fang et al. (2017), the coincidence of $\sqrt{\langle u'^2 \rangle}$ and $-\langle u' \cdot v' \rangle$ peaks can be explained by an energy transfer from the mean flow to the streamwise Reynolds normal stress $\langle u'^2 \rangle$ via the *TKE* production which is predominately caused by the interaction of the primary mean shear rate $\partial \langle u \rangle / \partial y$ and the Reynolds shear stress $-\langle u' \cdot v' \rangle$. Figures 9 and 10 suggested that local maxima of $-\langle u' \cdot v' \rangle$ were slightly below $y/k = 1.0$ between $x/k = 2.0$ and 4.0 and $\sqrt{\langle v'^2 \rangle}$ peaks were in the region of $y/k < 1.0$ between $x/k = 1.0$ and 5.0 . These findings were consistent with former studies in rib-roughened channels. Coletti et al. (2013) showed that $\sqrt{\langle v'^2 \rangle}$ peaks occurred in the border region between the separated shear layer and the recirculation region and at the rib leading edge. Liou et al. (1993) and Wang et al. (2007) reported that the maximum Reynolds shear stress occurred within the separated shear layer near $y/k = 1.0$. The closeness between the locations of $\sqrt{\langle u'^2 \rangle}$ and $\sqrt{\langle v'^2 \rangle}$ peaks within the inter-rib spacing can be explained by the energy redistribution from $\langle u'^2 \rangle$ toward

$\langle v'^2 \rangle$. Similarly to the results presented by Cui et al. (2003), high $\sqrt{\langle v'^2 \rangle}$ and $-\langle u' \cdot v' \rangle$ values were found near the rib leading edge. The enhanced Reynolds shear stress above the rib leading edge ($x/k = 7.9$) can be associated with diffusional transport which was triggered by bursts (Wang et al. (2010)), while the maximum of standard deviation of the wall-normal velocity originated in the enhanced mean shear rate of $\langle v \rangle$. An upward shift of $\sqrt{\langle v'^2 \rangle}$ and $-\langle u' \cdot v' \rangle$ peaks occurred along the rib crest (between $x/k = 7.9$ and 0.1), while local maxima were additionally generated within the developing shear layer immediately above the rib surface. The upward drift was not found for $\sqrt{\langle u'^2 \rangle}$. As shown for turbulent boundary layer flows over rough walls by Krogstad and Antonia (1999), $\langle v'^2 \rangle$ is more sensitive to turbulent diffusion than $\langle u'^2 \rangle$ and, thus, it is assumed that diffusional transport contributes substantially to Reynolds stresses in the region above the rib crest.

5.5 Turbulence kinetic energy

The turbulence kinetic energy $TKE = (\langle u'^2 \rangle + \langle v'^2 \rangle)/2$ followed the Reynolds normal stresses. *TKE* distributions normalized by the squared bulk velocity u_B^2 are shown in Fig. 11. They increased toward the rib-roughened wall. Consistent with the PIV results found by Cardwell et al. (2011) for Reynolds numbers of $Re_H = 1.0 \cdot 10^4$ and $2.0 \cdot 10^4$, *TKE* peaks occurred within the separated shear layer and varied only a little with the Reynolds number. The highest levels were found slightly above the rib trailing edge at $x/k = 0.1$, while local *TKE* maxima were located below $y/k = 1.0$ at $x/k = 2.0$ and 3.0 and above $y/k = 1.0$ further downstream. According to the Reynolds normal stress distributions, the distance of the *TKE* maxima from the channel bottom wall increased within the post-reattachment region ($x/k \geq 4$). Above $y/k \geq 3$, *TKE* was similarly distributed in the wall-normal direction and independent of the streamwise position.

To analyze the *TKE* transport mechanism in the rib-roughened channel, the simplified governing equation of *TKE*

$$\begin{aligned} \langle v \rangle \cdot \frac{\partial TKE}{\partial y} &= -\langle u'^2 \rangle \cdot \frac{\partial \langle u \rangle}{\partial x} - \langle v'^2 \rangle \cdot \frac{\partial \langle v \rangle}{\partial y} \\ &- \langle u' \cdot v' \rangle \cdot \frac{\partial \langle u \rangle}{\partial y} - \frac{1}{2} \cdot \frac{\partial}{\partial y} [\langle u'^2 \cdot v' \rangle + \langle v'^3 \rangle] \\ &+ v \cdot \frac{\partial^2 TKE}{\partial y^2} - \epsilon \end{aligned}$$

was considered, with the dissipation rate ϵ . In Fig. 12, the contributions to *TKE* from the wall-normal mean convection $C = \langle v \rangle \cdot \partial TKE / \partial y$, the turbulent diffusion $T = -1/2 \cdot \partial / \partial y [\langle u'^2 \cdot v' \rangle + \langle v'^3 \rangle]$, and the production $P = -\langle u'^2 \rangle \cdot \partial \langle u \rangle / \partial x - \langle v'^2 \rangle \cdot \partial \langle v \rangle / \partial y - \langle u' \cdot v' \rangle \cdot \partial \langle u \rangle / \partial y$ for $Re_H = 5.0 \cdot 10^4$ are shown (similar distributions were obtained for $Re_H = 1.0 \cdot 10^5$; not presented). The streamwise gradient of the mean streamwise velocity of the production

Fig. 12 Normalized contributions to *TKE* distributed in the wall-normal direction at different streamwise positions for $Re_H = 5.0 \cdot 10^4$. Grey symbols *C*, unfilled symbols *P* and black symbols *T*

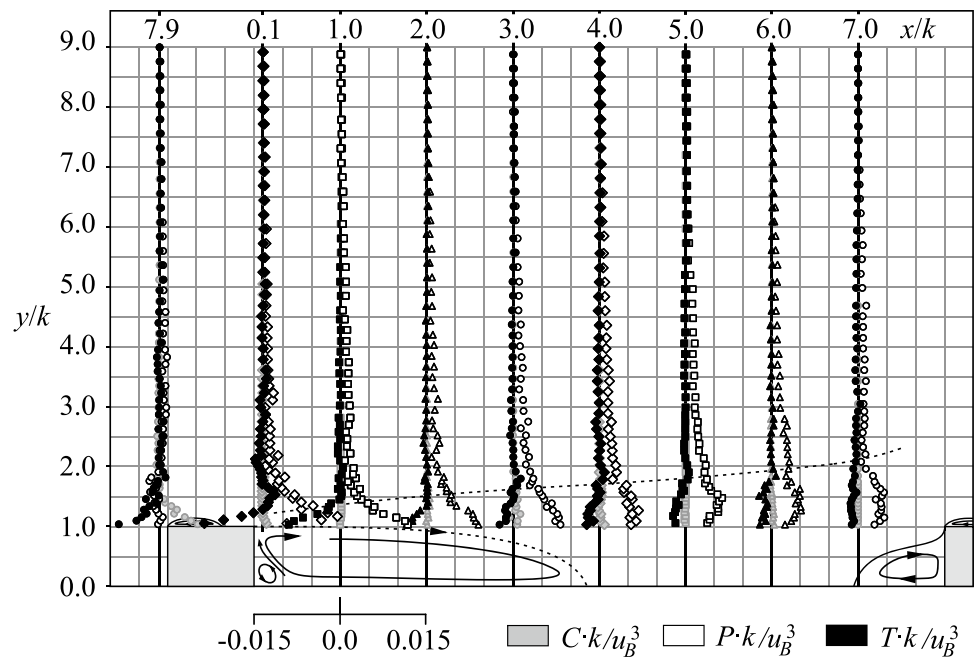
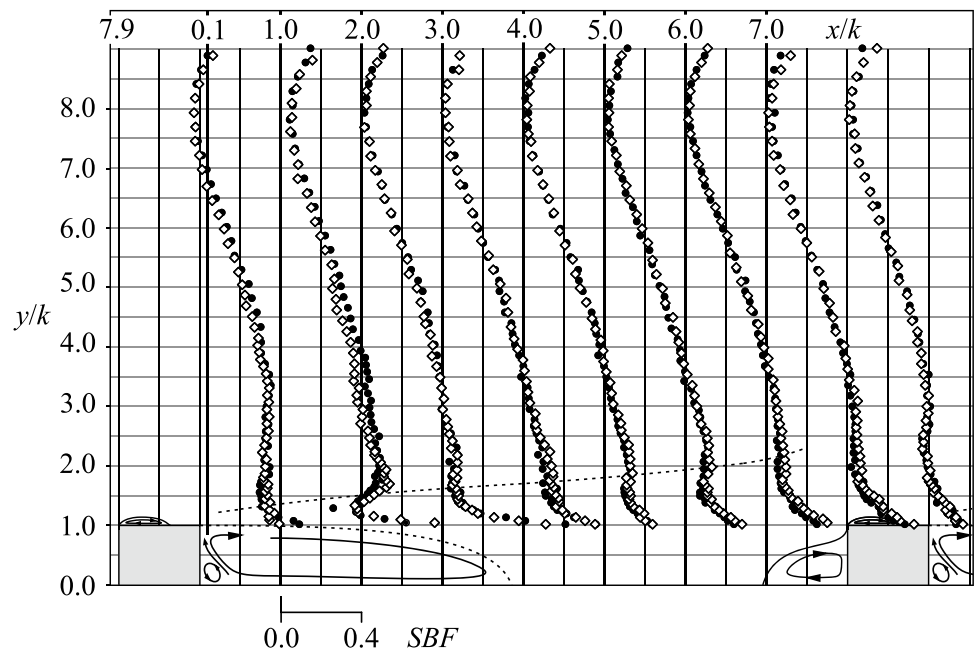


Fig. 13 Ratio between the contributions from the fourth and second quadrant to the Reynolds shear stress at different streamwise positions: “Diamond” $Re_H = 5.0 \cdot 10^4$ and “filled-circle” $Re_H = 1.0 \cdot 10^5$



term was approximated by the wall-normal gradient of the mean wall-normal velocity $\langle v \rangle$. Yokosawa et al. (1989) and Hirota et al. (1992) showed that the mean pattern of first- and second-order statistical moments of the velocity in a plane perpendicular to the channel axis (here the z - y plane) was symmetrically distributed with reference to the channel center plane (here the x - y plane at $z/k = 0$). Fang et al. (2015) reported that the spanwise gradient of the mean spanwise velocity in a one-sided rib-roughened channel was relatively small along the channel center plane.

Since the LDA measurements were carried out within the channel center plane, spanwise mean flow was assumed to be negligibly small, and thus, $-\partial \langle v \rangle / \partial y$ was used for $\partial \langle u \rangle / \partial x$ in the production term due to continuity. The viscous diffusion $v \cdot \partial^2 TKE / \partial y^2$ of *TKE* in wall-normal direction was very small for both Reynolds numbers when compared with the contributions from turbulent diffusion, convection, and production, and thus, it is not presented in Fig. 12. The dissipation rate and pressure diffusion can not be measured with the applied technique. The pressure diffusion for the

TKE transport was assumed to be comparable small, which is consistent with the three-dimensional DNS results for low Reynolds number turbulent flow in regions above the ribs in one-sided rib-roughened two-dimensional or square channels (Ikeda and Durbin (2007), Mahmoodi-Jezeh and Wang (2020)).

From the leeward rib surface to $x/k = 7.0$, the contribution from mean convection to *TKE* was negligibly small which is similar to the findings by Hirota et al. (1992) for rib-roughened channels with 60% lower relative roughness. The upward flow motion in front of the rib resulted in an enhancement of the mean convective transport of *TKE*. Above the rib leading edge, the magnitudes of mean convective and diffusional transport were comparable and larger than the contribution from the *TKE* production.

The high mean shear rates above and behind the rib drove the *TKE* production. *TKE* production peaks were generated within the separated shear layer close to the peak wall-normal gradients of the mean streamwise velocity. Immediately behind the rib, a local maximum occurred slightly above $y/k = 1.0$, while in the range from $x/k = 1.0$ to 3.0, local production maxima were expected to be below the rib height at the location of $\partial^2\langle u \rangle / \partial y^2 = 0$ (Fig. 5). In the post-reattachment region, *TKE* production peaks decreased. In accordance with the PIV results presented by Fang et al. (2015) and Wang et al. (2007), who investigated the flow in a one-sided rib-roughened square channel at Reynolds numbers of $Re_H = 1.15 \cdot 10^4$ and $2.2 \cdot 10^4$, respectively, the *TKE* production was governed by the primary mean shear rate in the separated shear layer. The contribution to *TKE* was almost always positive. Within the inter-rib spacing, the term $-\langle u' \cdot v' \rangle \cdot \partial\langle u \rangle / \partial y$ was up to two orders of magnitude higher than $-\langle v'^2 \rangle \cdot \partial\langle v \rangle / \partial y$ or $\langle u'^2 \rangle \cdot \partial\langle v \rangle / \partial y$. Here, $\langle u'^2 \rangle$ made larger contributions than $\langle v'^2 \rangle$ which was consistent with the Reynolds normal stress distributions in Figs. 8 and 9. At the rib leading and trailing edges, the abrupt change in the mean wall-normal velocity caused a large negative production by the Reynolds normal stress with the gradient of mean wall-normal velocity which reduced the positive contribution from the Reynolds shear stress with the primary mean shear rate and resulted into a *TKE* production decrease. Due to the results of Hirota et al. (1992), it can be assumed that the non-resolved spanwise contribution from the production to the *TKE* was small for the presented rib and flow configurations.

Turbulent diffusion plays an important role for the turbulent transport in rough-wall turbulent boundary layers (Andreopoulos and Bradshaw (1981), Krogstad and Antonia (1999), Keirsbulck et al. (2002)) and in rib-roughened channel flows (Hanjalić and Launder (1972), Mahmoodi-Jezeh and Wang (2020)). Despite the non-resolved spanwise contributions for the present case, it can be certainly

supposed that turbulent diffusion contributed significantly to *TKE* budget in the region $y/k \leq 2.0$. The contributions of $\langle u'^2 \cdot v' \rangle$ and $\langle v'^3 \rangle$ to turbulent diffusion were nearly of the same orders of magnitude. The amount of $\partial\langle v'^3 \rangle / \partial y$ was only considerably larger than $\partial\langle u'^2 \cdot v' \rangle / \partial y$ at the rib leading edge. Local maxima of wall-normal turbulent diffusion and production of *TKE* at $x/k = 0.1$ and 1.0 showed the same orders of magnitude. The high level of turbulent diffusion at $x/k = 1.0$ reduced further downstream and was almost vanished before it started to increase again in the proximity of the subsequent rib. At the rib leading edge, turbulent diffusion exceeded production and increased along the rib crest. It can be assumed that *TKE* produced just above the rib crest is substantially diffused outwards, which is consistent with the findings from the measured Reynolds stresses (Figs. 8, 9, 10) and with the DNS results described by Ikeda and Durbin (2007) who investigated the turbulent flow in a rib-roughened two-dimensional channel with comparable relative roughness at lower Reynolds numbers. From the presented results, it is obvious that turbulent diffusion in addition to mean vertical convection caused the outward drift of $\sqrt{\langle v'^2 \rangle}$ peaks between rib leading and trailing edges (Fig. 9).

The primary mean shear governed the $\langle u'^2 \rangle$ and *TKE* production (Fang et al. (2015)). Therefore, the non-coincidence of the *TKE* peaks (Fig. 11) or $\sqrt{\langle u'^2 \rangle}$ (Fig. 8) peaks and the local maxima of $\partial\langle u \rangle / \partial y$ (Fig. 5) in the region between $x/k = 1.0$ and $x/k = 3.0$ was attributed to diffusional transport of *TKE* which was generated during the streamwise development of the shear layer. As shown later by quadrant analysis, this behavior corresponds to the turbulent transport of Reynolds stresses induced by ejection and sweep events.

On the assumption of negligible pressure diffusion for the *TKE* transport and negligibly small *TKE* transport in spanwise direction, an equilibrium between the *TKE* production and dissipation was supposed to be established above the location where turbulent diffusion and mean convection vanished. Therefore, the vanishing diffusion as well as convection defined the demarcation line between the inner roughness layer and the outer equilibrium flow. For all streamwise positions, the turbulent diffusion of *TKE* settled down to zero in the range of $1.5 \leq y/k \leq 2.0$, while the significant *TKE* production vanished between $y/k = 5.0$ and 6.0.

5.6 Conditional averaged Reynolds shear stress

The intermittent eruption of decelerated fluid away from the wall (ejection event) and the following downward high-speed fluid motion (sweep event) play a crucial role for the Reynolds shear stress development and turbulent transport near rough and ribbed walls (Keirsbulck et al. (2002),

Krogstad et al. (2005), Fang et al. (2015)). By means of the quadrant analysis introduced by Wallace et al. (1972), both events can be quantified. Here, the instantaneous Reynolds shear stress $u' \cdot v'$ specifies ejection events for $u' < 0, v' > 0$ and sweep events for $u' > 0, v' < 0$. The second quadrant (Q_2) and fourth quadrant (Q_4) of the corresponding histogram plot represent each event graphically. In the present analysis, the contribution to $\langle u' \cdot v' \rangle$ from the j -th quadrant ($\langle u' \cdot v' \rangle_{Q_j}$) were determined by the conditional averaged Reynolds shear stress as proposed by Lu and Willmarth (1973). Similar to two-dimensional rib-roughened channel flow (Krogstad et al. (2005)) and rough-wall turbulent boundary layer flow (Keirsbulck et al. (2002)), the ejection events (Q_2) and sweep events (Q_4) were the main contributors to the Reynolds shear stress. To highlight the role of sweep and ejection events for the Reynolds shear stress generation and the associated turbulent transport, the distributions of the Sweep-Burst-Factor $SBF = \langle u' \cdot v' \rangle_{Q_j} / \langle u' \cdot v' \rangle_{Q_2}$ along the channel center plane are depicted in Fig. 13. The wall-normal distributions show the same trends for both Reynolds numbers and are almost independent of the streamwise position for $y/k > 4.0$ near the rib and for $y/k > 2.0$ between $x/k = 1.0$ and 6.0 . Above the rib leading and trailing edges ($x/k = 7.9$ and 0.1) the dominate contribution from the Q_2 quadrant ($SBF < 1.0$) indicated enhanced turbulent transport of energy from the wall toward the channel core. Local minima of SBF coincided with Reynolds shear stress peaks (Fig. 10). For both Reynolds numbers, the Reynolds shear stress increase at this region was mainly driven by the turbulence transport of the intermittent bursts as shown for lower Reynolds number flows by Wang et al. (2010) and Cardwell et al. (2011). Since the occurrence of intense ejection events near the rib corresponded to the regions where turbulent diffusion of TKE peaked, ejection events can be considered as the major contributor to the turbulent diffusion (Fig. 11) and as the driver for the revealed outward shift of Reynolds stresses. Behind the rib, ejection and sweep events originated in the shear layer flapping. Flow structures generated with the shear layer were ejected outwards and the following fluid extracted from the downward directed fluid of the core flow swept toward the wall within the inter-rib spacing. Considerable sweep events were reflected in the increased $SBF > 1.0$ slight above the rib height between $x/k = 1.0$ and $x/k = 7.0$. Both events developed with the shear layer within the inter-rib spacing. In accordance with the distribution of turbulent diffusion of TKE , they became weaker further downstream before the reduction in the SBF indicated the increase in ejection events near the subsequent rib.

6 Conclusion

LDA measurements in the fully developed turbulent flow regime of a one-sided rib-roughened square channel were carried out to investigate the turbulent flow at Reynolds numbers of $Re_H = 5.0 \cdot 10^4$ and $1.0 \cdot 10^5$. Mean velocities, Reynolds normal, and shear stresses as well as TKE showed some similarities to flows in a two-dimensional or square channel with k -type roughness at lower Reynolds numbers and higher or lower relative roughness. The statistical moments exhibited a slight Reynolds number dependency when normalized by the bulk velocity and the channel height. The Reynolds number dependency was mainly restricted to a layer above the ribs, while outside the layer, the distributions of statistical moments in wall-normal direction were independent of the streamwise position and Reynolds number. Deviations with increasing Reynolds numbers were based on the minor elongation increase in the recirculation region, which was found from the derived reattachment length. Effects of the Reynolds number on the velocity field as well as on turbulence transport phenomena seem to be less significant for the analysed Reynolds numbers range of $5.0 \cdot 10^4 \leq Re_H \leq 1.0 \cdot 10^5$ when compared with the influence of rib pitch or rib roughness variations. However, from the results, it can be assumed that the elongation increase in the large recirculation region behind the rib displaces the boundary between the k -type and intermediate roughnesses to higher rib pitches at very high Reynolds numbers which would result in a completely different flow field.

Reynolds stresses were enhanced by the ribs. Maximum Reynolds stresses occurred at the rib crest or were located within the inter-rib spacing beneath the rib height. Ejection events contribute pivotally the Reynolds shear stress slight above the rib leading and trailing edges. Despite the primary mean shear governed by the $\langle u'^2 \rangle$ production and TKE production, locations of $\sqrt{\langle u'^2 \rangle}$ peaks and the inflection points of the mean streamwise velocity behind the rib did not match. The non-coincidence was attributed to diffusional transport driven by ejections and sweep events. The upward shift of the $\sqrt{\langle v'^2 \rangle}$ peak between the rib leading and trailing edges along the rib crest was apparently caused by diffusional and mean convective transport. Here, strong ejection events indicated enhanced diffusional transport of TKE away from the wall toward the channel core. From a simplified governing equation of TKE , it was found that turbulent diffusion contributed significantly to TKE budget near the rib and within the separated shear layer in the pre-reattachment region. An equilibrium between TKE production and dissipation was assumed to be absent within a layer of 1 to 2 k height above the rib. Immediately behind the rib, TKE production was balanced by turbulent diffusion, while above the rib leading edge, the mean convection and

turbulent diffusion of *TKE* balanced each other and their magnitudes exceeded the *TKE* production.

The large contribution of turbulent diffusion to the *TKE* budget highlights its importance for computations of turbulent flow in similarly structured rib-roughened channels. The time-averaged data reported here provide an appropriate basis for a thorough validation of calculation methods and model approaches. It should be noted that the flow field of the presented data is inhomogeneous in all directions. Viscous effects from the wall-bounded shear layers of the lateral sidewalls as well as strong secondary flows of the first and second kind in the spanwise-wall-normal direction affect the complete flow field and can lead to substantial difference compared to two-dimensional flow configurations. The prepared data can be obtained for validation studies from the corresponding author and from the KITopen repository at <https://doi.org/10.5445/IR/1000137380>.

Funding Open Access funding enabled and organized by Projekt DEAL.

Declarations

Conflict of interest The authors declare that they have no conflict of interest.

Open Access This article is licensed under a Creative Commons Attribution 4.0 International License, which permits use, sharing, adaptation, distribution and reproduction in any medium or format, as long as you give appropriate credit to the original author(s) and the source, provide a link to the Creative Commons licence, and indicate if changes were made. The images or other third party material in this article are included in the article's Creative Commons licence, unless indicated otherwise in a credit line to the material. If material is not included in the article's Creative Commons licence and your intended use is not permitted by statutory regulation or exceeds the permitted use, you will need to obtain permission directly from the copyright holder. To view a copy of this licence, visit <http://creativecommons.org/licenses/by/4.0/>.

References

- Ahn J, Choi H, LJ S (2005) Large Eddy simulation of flow and heat transfer in a channel roughened by square or semicircle ribs. *J Turbomach* 172(2):263–269. <https://doi.org/10.1115/1.1811098>
- Andreopoulos J, Bradshaw P (1981) Measurements of turbulence structure in the boundary layer on a rough surface. *Bound-Layer Meteorol* 20:201–213. <https://doi.org/10.1007/BF00119902>
- Bandyopadhyay PR (1987) Rough-wall turbulent boundary layers in the transition regime. *J Fluid Mech* 180:231–266. <https://doi.org/10.1017/S0022112087001794>
- Benedict L, Gould R (1996) Towards better uncertainty estimates for turbulence statistics. *Exp Fluids* 22:129–136. <https://doi.org/10.1007/s003480050030>
- Cakan M (2000) Aero-thermal investigation of fixed rib-roughened cooling passages. Dissertation, Université Catholique de Louvain. von Karman Institute for Fluid Dynamics

- Cardwell ND, Vlachos PP, Thole KA (2011) Developing and fully developed turbulent flow in ribbed channels. *Exp Fluids* 50:1357–1371. <https://doi.org/10.1007/s00348-010-0993-y>
- Casarsa L, Arts T (2005) Experimental investigation of the aerothermal performance of a high blockage rib-roughened cooling channel. *J Turbomach* 127:580–588. <https://doi.org/10.1115/1.1928933>
- Coletti F, Cresci I, Arts T (2013) Spatio-temporal analysis of the turbulent flow in a ribbed channel. *Int J Heat Fluid Flow* 44:181–196. <https://doi.org/10.1016/j.ijheatfluidflow.2013.05.020>
- Cui J, Patel VC, Lin CL (2003) Large-eddy simulation of turbulent flow in a channel with rib roughness. *Int J Heat Fluid Flow* 24(3):372–388. [https://doi.org/10.1016/S0142-727X\(03\)00002-X](https://doi.org/10.1016/S0142-727X(03)00002-X)
- Fang X, Yang Z, Wang BC, Tachie MF, Bergstrom DJ (2015) Highly-disturbed turbulent flow in a square channel with v-shaped ribs on one wall. *Int J Heat Fluid Flow* 56:182–197. <https://doi.org/10.1016/j.ijheatfluidflow.2015.07.008>
- Fang X, Yang Z, Wang BC, Tachie MF, Bergstrom D (2017) Large-eddy simulation of turbulent flow and structures in a square duct roughened with perpendicular and v-shaped ribs. *Phys Fluids* 29(6):065110. <https://doi.org/10.1063/1.4985715>
- George WK, Beuther PD, Lumley JL (1978) Processing of random signals. pp 757–800
- Graham A, Sewall E, Thole KA (2004) Flowfield measurements in a ribbed channel relevant to internal turbine blade cooling. *Turbo expo: power for land, sea, and air, vol Volume 3: turbo expo 2004*, pp 383–391. <https://doi.org/10.1115/GT2004-53361>
- Han JC (2004) Recent studies in turbine blade cooling. *Int J Rotating Mach* 10(6):443–457
- Hanjalić K, Launder BE (1972) Fully developed asymmetric flow in a plane channel. *J Fluid Mech* 51(2):301–335. <https://doi.org/10.1017/S0022112072001211>
- Hans VS, Saini RP, Saini JS (2009) Performance of artificially roughened solar air heaters—a review. *Renew Sustain Energy Rev* 13(8):1854–1869. <https://doi.org/10.1016/j.rser.2009.01.030>
- Hirota M, Yokosawa H, Fujita H (1992) Turbulence kinetic energy in turbulent flows through square ducts with rib-roughened walls. *Int J Heat Fluid Flow* 13(1):22–29. [https://doi.org/10.1016/0142-727X\(92\)90056-F](https://doi.org/10.1016/0142-727X(92)90056-F)
- Hoyas S, Jiménez J (2006) Scaling of the velocity fluctuations in turbulent channels up to $re_\tau = 2003$. *Phys Fluids* 18(1):011702. <https://doi.org/10.1063/1.2162185>
- Ikeda T, Durbin P (2007) Direct simulations of a rough-wall channel flow. *J Fluid Mech* 571:235–263. <https://doi.org/10.1017/S002211200600334X>
- Islam MS, Haga K, Kaminaga M, Hino R, Monde M (2002) Experimental analysis of turbulent flow structure in a fully developed rib-roughened rectangular channel with PIV. *Exp Fluids* 33:296–306. <https://doi.org/10.1007/s00348-002-0432-9>
- Keirsbulck L, Labraga L, Mazouz A, Tournier C (2002) Surface roughness effects on turbulent boundary layer structures. *J Fluids Eng* 124(1):127–135. <https://doi.org/10.1115/1.1445141>
- Kline S, Mcclintock F (1953) Describing uncertainties in single-sample experiments. *Mechanical engineering, Mech Eng* 75:3–8. <https://doi.org/10.1017/S002211200600334X>
- Krogstad PA, Andersson HI, Bakken OM, Asharafian A (2005) An experimental and numerical study of channel flow with rough walls. *J Fluid Mech* 530:327–352. <https://doi.org/10.1017/S0022112005003824>
- Krogstadt P, Antonia R (1999) Surface roughness effects in turbulent boundary layers. *Exp Fluids* 27:450–460. <https://doi.org/10.1007/s003480050370>
- Labbé O (2013) Large-eddy-simulation of flow and heat transfer in a ribbed duct. *Comput Fluids* 76:23–32. <https://doi.org/10.1016/j.compfluid.2013.01.023>
- Leonardi S, Orlandi P, Smalley R, Djenidi L, Antonia RA (2003) Direct numerical simulations of turbulent channel flow with transverse

- square bars on one wall. *J Fluid Mech* 491:229–238. <https://doi.org/10.1017/S0022112003005500>
- Liou T, Wu Y, Chang Y (1993) LDV measurements of periodic fully developed main and secondary flows in a channel with rib-disturbed walls. *J Fluids Eng* 115(1):109–114. <https://doi.org/10.1115/1.2910091>
- Liou TM, Hwang JJ, Chen SH (1992) Turbulent transport phenomena in a channel with periodic rib turbulators. *J Thermophys Heat Trans* 6:513–521. <https://doi.org/10.2514/3.390>
- Lu SS, Willmarth WW (1973) Measurements of the structure of the Reynolds stress in a turbulent boundary layer. *J Fluid Mech* 60(3):481–511. <https://doi.org/10.1017/S0022112073000315>
- Mahmoodi-Jezeh SV, Wang BC (2020) Direct numerical simulation of turbulent flow through a ribbed square duct. *J Fluid Mech* 900:A18. <https://doi.org/10.1017/jfm.2020.452>
- Nobach H, Tropea C (2007) Fundamentals of data processing. In: Tropea C, Yarin AL, Foss JF (eds) *Handbook of experimental fluid mechanics*. Springer-Verlag, Berlin Heidelberg. <https://doi.org/10.1007/978-3-540-30299-5>
- Okamoto S, Seo S, Nakaso K, Kawai I (1993) Turbulent shear flow and heat transfer over the repeated two dimensional square ribs on ground plane. *J Fluids Eng* 115(4):631–637. <https://doi.org/10.1115/1.2910191>
- Perry AE, Schofield WH, Joubert PN (1969) Rough wall turbulent boundary layers. *J Fluid Mech* 37(2):383–413. <https://doi.org/10.1017/S0022112069000619>
- Petukhov BS (1970) Heat transfer and friction in turbulent pipe flow with variable physical properties. *Adv Heat Transf* 6:523. [https://doi.org/10.1016/S0065-2717\(08\)70153-9](https://doi.org/10.1016/S0065-2717(08)70153-9)
- Rau G, Cakan M, Moeller D, Arts T (1998) The effect of periodic ribs on the local aerodynamic and heat transfer performance of a straight cooling channel. *J Turbomach* 120:368–375. <https://doi.org/10.1115/1.2841415>
- Raupach MR, Antonia RA, Rajagopalan S (1991) Rough-wall turbulent boundary layers. *Appl Mech Rev* 44(1):1–25. <https://doi.org/10.1115/1.3119492>
- Ruck B (1990) *Lasermethoden in der Strömungsmesstechnik*. AT Fachverlag GmbH Stuttgart
- Ruck S, Arbeiter F, Brenneis B, Hernandez F, Neuberger H, Schwab F (2019) Thermal-hydraulic study on rib and dimple structures for cooling the First Wall of DEMO. *Fusion Eng Des* 146:2144–2148. <https://doi.org/10.1016/j.fusengdes.2019.03.125>
- Sewall EA, Tafti DK (2004) Large eddy simulation of the developing region of a stationary ribbed internal turbine blade cooling channel. *Turbo expo: power for land, sea, and air, vol 3: turbo expo 2004*, pp 735–747. <https://doi.org/10.1115/GT2004-53832>
- Stukel J, Hopke P, Nourmohammadi K (1984) Turbulent air flow over rough surfaces: mean flow parameters. *J Fluids Eng* 106(4). <https://doi.org/10.1115/1.3243138>
- Tennekes H, Lumley JL (1972) *A first course in turbulence*. MIT Press, Cambridge, Massachusetts and London
- VDI (2010) *VDI heat Atlas*, 2nd edn. Springer-Verlag, Berlin Heidelberg
- Wallace JM (2016) Quadrant analysis in turbulence research: history and evolution. *Annu Rev Fluid Mech* 48(1):131–158. <https://doi.org/10.1146/annurev-fluid-122414-034550>
- Wallace JM, Eckelmann H, Brodkey RS (1972) The wall region in turbulent shear flow. *J Fluid Mech* 54(1):39–48. <https://doi.org/10.1017/S0022112072000515>
- Wang L, Hejicik J, Sundén B (2007) PIV measurement of separated flow in a square channel with streamwise periodic ribs on one wall. *J Fluids Eng* 129:834–841. <https://doi.org/10.1115/1.2742723>
- Wang L, Salewski M, Sundén B (2010) Turbulent flow in a ribbed channel: flow structures in the vicinity of a rib. *Exp Therm Fluid Sci* 34:165–176. <https://doi.org/10.1016/j.expthermflusci.2009.10.005>
- Yokosawa H, Fujita H, Hirato M, Iwata S (1989) Measurement of turbulent flow in a square duct with roughened walls on two opposite sides. *Int J Heat Fluid Flow* 10(2):125–130. [https://doi.org/10.1016/0142-727X\(89\)90005-2](https://doi.org/10.1016/0142-727X(89)90005-2)

Publisher's Note Springer Nature remains neutral with regard to jurisdictional claims in published maps and institutional affiliations.